Imaging magnetic scalar potentials by laser-induced fluorescence from bright and dark atoms

I Fescenko[1,2] and A Weis[1]

[1] Physics Department, University of Fribourg, Chemin du Musée 3, 1700 Fribourg, Switzerland
[2] Institute of Atomic Physics and Spectroscopy, University of Latvia, 19 Rainis Boulevard, LV-1586 Riga, Latvia

E-mail: iliafes@gmail.com

Abstract

We present a spectroscopic method for mapping two-dimensional distributions of magnetic field strengths (magnetic scalar potential lines) using charge-coupled device (CCD) recordings of the fluorescence patterns emitted by spin-polarized Cs vapour in a buffer gas exposed to inhomogeneous magnetic fields. The method relies on the position-selective destruction of spin polarization by magnetic resonances induced by multi-component oscillating magnetic fields, such that magnetic potential lines can be directly detected by the CCD camera. We also present a generic algebraic model allowing for the calculation of the fluorescence patterns and find excellent agreement with the experimental observations for three distinct inhomogeneous field topologies. The spatial resolution obtained with these proof-of-principle experiments is of the order of 1 mm. A substantial increase of spatial and magnetic field resolution is expected by deploying the method in a magnetically shielded environment.

Keywords: magneto-optical effects, magnetic field imaging, caesium

1. Introduction

The use of inhomogeneous magnetic fields for encoding inhomogeneous distributions of spin-polarized particles into a (Larmor) frequency spectrum is the underlying principle of magnetic resonance imaging (MRI). In this paper we apply the converse of this procedure by using a homogeneous distribution of polarized particles for imaging inhomogeneous magnetic field distributions. In the reported proof-of-principle experiments we demonstrate that the method yields high quality images of magnetic potential lines produced by known sources. While conventional medical MRI relies on detecting the relevant Larmor frequency spectrum by pick-up coils, the imaging sensor described here uses a spin-polarized alkali atom vapour in combination with optical detection.

Our research is motivated by two main objectives. On one hand we wanted to develop a simple lecture demonstration experiment for visualizing dark atomic states, hence the fact that the experiment was carried out in a magnetically

unshielded environment offering visibility of all experimental components. On the other hand, we are currently developing means for imaging magnetic nanoparticles embedded in biological tissues in view of biomedical applications. While the proof-of-principle experiments reported below fully satisfy the first objective, they constitute a first step towards the second objective that aims at imaging inhomogeneous nanoparticle distributions via the inhomogeneous magnetic field patterns that they produce. A magnetic field imaging camera based on this principle will open new pathways for quantitative space- and time-resolved studies of the distribution and dynamics of nanoparticles in biological samples.

2. Method

It is well known that the optical absorption coefficient of an atomic ensemble depends on the degree and nature of its spin polarization. In general, the creation of spin polarization by optical pumping with (resonant) polarized light reduces

the absorption coefficient of an atomic medium, which thus becomes more transparent for the pumping light. This effect is a manifestation of electromagnetically induced transparency (EIT) that goes in pair with a reduction of atomic fluorescence, a fact which is commonly expressed by stating that the polarized medium is in a dark state. Dark atomic ensembles are also said to be in a coherent population trapped (CPT) state since optical pumping creates a coherent superposition of (Zeeman or hyperfine) magnetic sublevels, with amplitudes and phases such that the incident polarized light does not couple to that particular superposition state. The seminal paper by Alzetta *et al* [1] nicely illustrated the concept of (non-absorbing) dark states by photographic recordings of their reduced fluorescence.

Imaging inhomogeneous distributions of spin-polarized atoms have been used in the past for space–time resolved studies of atomic diffusion [2–4]. Magnetic iso-field lines were mapped for the first time by Tam and Happer [5] by photographic recordings of fluorescence from Na vapour excited by a multi-frequency optical field (frequency comb) in homogeneous and inhomogeneous fields. They applied the technique for the visual analysis of optical rf spectra [5, 6]. More recently quantitative digital methods based on charge-coupled device (CCD) cameras were deployed for field imaging in fluorescence [7] and transmission [8] experiments. In contrast to previous field mapping experiments that used bi- or poly-chromatic optical fields to prepare non-absorbing (non-fluorescing) states our experiments use monochromatic laser radiation. Optical pumping with *linearly polarized* light on the $F_g = 4 \rightarrow F_e = 3$ component of the Cs D_1 transition creates spin alignment oriented along the direction of light polarization, while pumping with *circularly polarized* light prepares both vector polarization (orientation) and tensor polarization (alignment) along the light propagation direction $\hat{k}$, the alignment contribution being negligible compared to the orientation on that specific hyperfine transition [9]. A static magnetic field applied to a polarized medium affects the degree and orientation of the medium's polarization, an effect known as ground state Hanle effect (GSHE). Since the fluorescence intensity depends both on the magnetic field amplitude and its relative orientation with respect to the direction of spin polarization, an inhomogeneous magnetic field therefore produces a spatially varying fluorescence pattern (Hanle background pattern). Irradiating the sample in the inhomogeneous magnetic field additionally with a mono- or poly-chromatic rf field will depolarize the sample at spatial locations where the local Larmor frequency matches the rf frequency, thereby lighting up the regions with a specific modulus of the magnetic field strength. In this way, the recording of the fluorescence patterns by a CCD camera allows the mapping of magnetic potential lines.

3. Laser-induced fluorescence of spin-polarized atoms

The power of fluorescence light induced by a resonant laser of power P_0 traversing a *spin-oriented* atomic vapour is given by

$$\mathrm{d}P_\mathrm{f}^{(1)} = P_0\, \kappa_0 L\, (1 - \alpha^{(1)} m_{1,0})\, f^{(1)}(\Omega)\, \mathrm{d}\Omega, \qquad (1)$$

where κ_0 is the peak optical absorption coefficient of the (in our case, Doppler-broadened) atomic absorption line, L the length of the illuminated vapour column imaged onto the fluorescence detector, and $\mathrm{d}\Omega$ the solid angle intercepted by the detector. The superscript (1) refers to $k = 1$ and denotes the vector character of the spin polarization (orientation). The function $f^{(1)}(\Omega)$ represents the angular distribution of the fluorescence intensity. Throughout the paper we will assume an isotropic distribution of fluorescence, thus choosing $f^{(1)}(\Omega)$ to be a constant. The parameter $\alpha^{(1)} = \alpha^{(1)}_{F_g, F_e}$ is the orientation analysing power introduced in [10], which depends on the angular momentum quantum numbers of the specific transition excited by the laser. We characterize spin orientation in terms of the longitudinal vector multipole moment $m_{1,0}$, the only anisotropy parameter of the medium to which circularly polarized light couples when the medium's alignment can be neglected.

With the above we can express the total fluorescence power recorded by the detector as

$$P_\mathrm{f}^{(1)} = \int \frac{\mathrm{d}P_\mathrm{f}^{(1)}}{\mathrm{d}\Omega}\, \mathrm{d}\Omega \equiv A^{(1)} \left(1 - \alpha^{(1)} m_{1,0}\right). \qquad (2)$$

In the same way, one can represent the fluorescence of spin-aligned atoms by

$$P_\mathrm{f}^{(2)} = \int \frac{\mathrm{d}P_\mathrm{f}^{(2)}}{\mathrm{d}\Omega}\, \mathrm{d}\Omega \equiv A^{(2)} \left(1 - \alpha^{(2)} m_{2,0}\right), \qquad (3)$$

where the atomic multipole moment $m_{2,0}$ is the longitudinal spin alignment that is oriented along the light polarization when produced by optical pumping with linearly polarized light. $\alpha^{(2)}$ is the alignment analysing power, introduced in [11].

3.1. Fluorescence of spin-oriented atoms in an inhomogeneous magnetic field

A magnetic field of arbitrary direction applied to the medium will change the magnitude and orientation of its spin polarization. It was shown in [10] that the steady-state value $m_{1,0}^\mathrm{ss}$ that the longitudinal orientation reaches by virtue of the GSHE is given by the Hanle function

$$\mu^{(1)}(\beta_\parallel, \beta_\perp) \equiv \frac{m_{1,0}^\mathrm{ss}}{m_{1,0}^\mathrm{eq}} = \frac{1 + \beta_\parallel^2}{1 + \beta_\parallel^2 + \beta_\perp^2}, \qquad (4)$$

where $\beta_\parallel$ and $\beta_\perp$ denote the longitudinal and transverse (with respect to $\vec{k}$) magnetic field components, expressed in dimensionless units according to

$$\beta_\parallel \equiv \frac{\omega_\parallel}{\gamma} = \frac{\gamma_F\, |\vec{B}_\parallel|}{\gamma} \quad \text{and} \quad \beta_\perp \equiv \frac{\omega_\perp}{\gamma} = \frac{\gamma_F\, |\vec{B}_\perp|}{\gamma}, \qquad (5)$$

where we have assumed identical longitudinal and transverse orientation relaxation rates ($\gamma_1 = \gamma_2 \equiv \gamma$). The Larmor frequencies $\omega_{\parallel, \perp}$ are related to the respective field components via the gyromagnetic ratio $\gamma_F \approx (2\pi)\, 3.5\, \mathrm{Hz\, nT^{-1}}$ of the Cs ground state. In equation (4), $m_{1,0}^\mathrm{eq}$ represents the longitudinal orientation that is achieved by optical pumping

in a polarization-stabilizing longitudinal field ($\beta_\parallel \gg \beta_\perp$), so that $\mu^{(1)}(\beta_\parallel, \beta_\perp)$ can assume values between 0 and 1.

When the atomic medium is exposed to an inhomogeneous magnetic field, $\beta_\parallel$ and $\beta_\perp$ depend on the position $\vec{r}$ in the atomic medium from which fluorescence is emitted, so that the florescence power emitted by a volume element (voxel) of the atomic medium located at $\vec{r}$ can be written as

$$P_f^{(1)}(\vec{r}) = A^{(1)} \left(1 - \alpha^{(1)} m_{1,0}^{eq} \mu^{(1)}(\beta_\parallel, \beta_\perp) \right) \qquad (6a)$$

$$\propto 1 - C^{(1)} \frac{1 + \beta_\parallel^2(\vec{r})}{1 + \beta_\parallel^2(\vec{r}) + \beta_\perp^2(\vec{r})}, \qquad (6b)$$

with

$$C^{(1)} = \frac{B^{(1)}}{A^{(1)}} = \frac{\alpha^{(1)} m_{1,0}^{eq}}{P_0 \kappa_0 L \int f^{(1)}(\Omega) d\Omega}. \qquad (7)$$

In the experiments reported below, we use a CCD camera for recording the fluorescence emitted from a quasi-two-dimensional volume excited by a sheet of laser light in a cubic vapour cell exposed to an inhomogeneous magnetic field. The light intensity distribution on the CCD chip can then be calculated by inserting the (known) spatial dependence of $\beta_\parallel(\vec{r})$ and $\beta_\perp(\vec{r})$ in the light emitting volume (located at position $\vec{r}$) into equation (6b).

3.2. Magnetic resonance induced modifications of the fluorescence from oriented atoms

Polarized atoms emit a weak fluorescence, while unpolarized atoms emit a stronger fluorescence. Local magnetic fields that are oriented along the axis of spin polarization stabilize the latter, so that voxels containing polarized atoms lead to darker parts in the CCD image. The experiments described below show that the models developed here yield a good quantitative prediction of the observed fluorescence from atoms in a variety of inhomogeneous fields. However, the inverse problem which consists in inferring the magnetic field distribution from the recorded fluorescence pattern is a more demanding task. Although this inverse problem may, in principle, be solved based on fluorescence images recorded with different (circular and linear) polarizations, we have not yet attempted to do so.

Rather than attempting to solve the inverse problem we present here a method allowing the easy visualization and measurement of magnetic potential lines. The method is based on the space-selective destruction of spin polarization by magnetic resonance. It is well known that a weak oscillating magnetic field $B_1 \cos(\omega_{rf} t)$, called 'rf'-field, resonantly modifies the magnetization (spin polarization) of a medium, when its oscillation frequency matches the Larmor frequency, i.e., when $\omega_{rf} = \omega_L(\vec{r})$, a phenomenon known as magnetic resonance. The steady-state solution of the Bloch equations (under the assumption of identical longitudinal and transverse relaxation rates) is given by [12]

$$m_{1,0} = m_{1,0}^{ss} \left(1 - \frac{\sqrt{S_{rf}}}{\delta^2 + S_{rf} + 1} \right) \qquad (8)$$

for the longitudinal spin orientation, with $\delta = (\omega_{rf} - \omega_L)/\gamma \equiv \beta_{rf} - \beta$, where γ is the polarization's relaxation rate. The rf saturation parameter S_{rf} is defined as

$$S_{rf} = \left(\frac{\gamma_F B_1}{\gamma} \right)^2 \equiv \beta_1^2. \qquad (9)$$

In equation (8), the multipole moment $m_{1,0}^{ss}$ represents the steady-state spin polarization established by the Hanle effect in absence of the rf field ($S_{rf} = 0$), given by equation (4). The orientation resulting from the joint depolarization by the inhomogeneous field and the rf field is thus given by

$$m_{1,0} = m_{1,0}^{eq} \frac{1 + \beta_\parallel^2}{1 + \beta_\parallel^2 + \beta_\perp^2} \left(1 - \frac{\sqrt{S_{rf}}}{\delta^2 + S_{rf} + 1} \right), \qquad (10)$$

and the fluorescence of equation (6a) becomes

$$P_f^{(1)}(\vec{r}) = A^{(1)} \left(1 - \alpha^{(1)} m_{1,0} \right) \qquad (11a)$$

$$= A^{(1)} \left[1 - \alpha^{(1)} m_{1,0}^{eq} \frac{1 + \beta_\parallel^2}{1 + \beta_\parallel^2 + \beta_\perp^2} \left(1 - \frac{\sqrt{S_{rf}}}{\delta^2 + S_{rf} + 1} \right) \right]$$
$$(11b)$$

$$= A^{(1)} - B^{(1)} \frac{1 + \beta_\parallel^2}{1 + \beta_\parallel^2 + \beta_\perp^2} \left(1 - \frac{\sqrt{S_{rf}}}{\delta^2 + S_{rf} + 1} \right) \qquad (11c)$$

$$\propto 1 - C^{(1)} \frac{1 + \beta_\parallel^2}{1 + \beta_\parallel^2 + \beta_\perp^2} \left(1 - \frac{\sqrt{S_{rf}}}{(\beta_{rf} - \beta)^2 + S_{rf} + 1} \right), \quad (11d)$$

which reduces to equation (6b) for $S_{rf} = 0$.

In an inhomogeneous field $\vec{\beta}(\vec{r}) = \vec{\beta}_\parallel(\vec{r}) + \vec{\beta}_\perp(\vec{r})$, the parameters $\beta_\parallel$, $\beta_\perp$, $\beta = \sqrt{\beta_\parallel^2 + \beta_\perp^2}$ in equation (11d) depend on $\vec{r}$, while $S_{rf} = \beta_1^2$ is assumed to be homogeneous. When the spin-polarized atomic medium in an inhomogeneous magnetic environment is irradiated with an rf field, this field will depolarize the medium at positions $\vec{r}$ at which the modulus β of the local magnetic field $\vec{\beta}$ obeys $\beta = \beta_{rf} = \omega_{rf}/\gamma_F$, so that these regions will light up with an enhanced intensity in the CCD image. When light from a plane in the vapour is imaged onto the CCD chip, it is possible in this way to visualize the lines of constant $|\vec{\beta}|$ in that plane.

Note that the lines of constant $|\vec{\beta}|$ represent the magnetic scalar potential $\Psi(\vec{r})$, from which the magnetic field (in current-free regions) can be derived via $\vec{B}(\vec{r}) = -\mu_0 \vec{\nabla} \Psi(\vec{r})$. Note also that throughout the paper we refer to the magnetic induction vector $\vec{B}$ as 'magnetic field' vector, following common laboratory practice.

3.3. Magnetic resonance induced fluorescence of spin-aligned atoms in an inhomogeneous magnetic field

Optical pumping with linearly polarized light produces a longitudinal alignment $m_{2,0}^{eq}$ that is oriented along the light polarization. In [11] it was shown that a magnetic field of arbitrary magnitude and orientation yields a steady-state magnetization $m_{2,0}^{ss}$ given by

$$\mu^{(2)}(\beta_\parallel, \beta_\perp) \equiv \frac{m_{2,0}^{ss}}{m_{2,0}^{eq}} = \frac{1}{4} + \frac{3}{4} \frac{1 + 8\beta_\parallel^2 + 16\beta_\parallel^4}{1 + 4\beta_\parallel^2 + 4\beta_\perp^2}$$
$$- 3 \frac{\beta_\parallel^2 + \beta_\parallel^4}{1 + \beta_\parallel^2 + \beta_\perp^2}, \qquad (12)$$
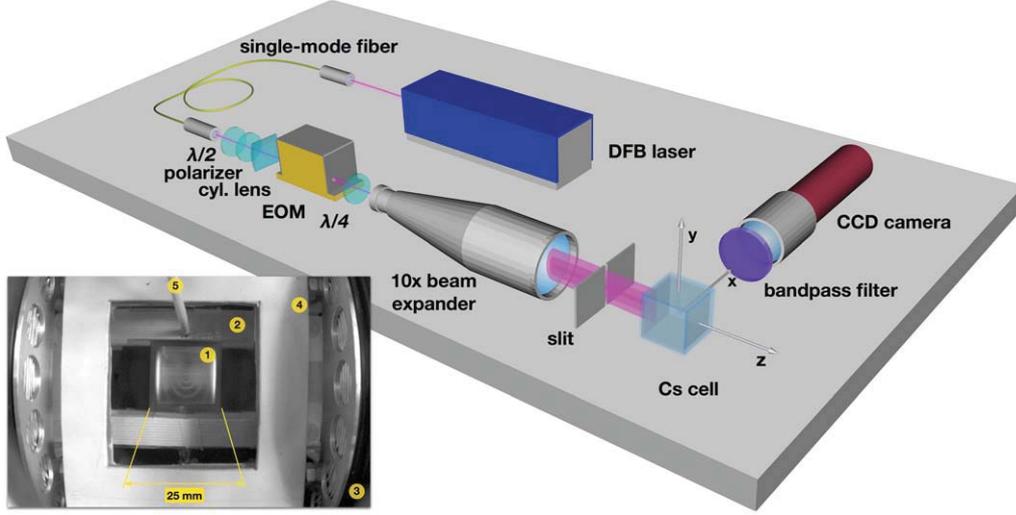
Figure 1. Schematic layout of the apparatus, not including magnetic field coils. The photograph shows the central part of the set-up, as seen by the CCD camera. One distinguishes: the cubic vapour cell (1) with ring-structured fluorescence produced by the 1 WH field configuration, one of the support structures for the rf coils (2), the coils producing the quadrupole field (3), a support structure for the eight wires of the 8W-configuration (4), and the protruding 'wire' of the 1 WH field configuration.

where $m_{2,0}^{\text{eq}}$ represents the longitudinal alignment, oriented along the laser polarization that is produced by optical pumping in a stabilizing $(\beta_{\parallel} \gg \beta_{\perp})$ field, and where $0 \leqslant \mu^{(2)} \leqslant 1$. Note that in the case of linearly polarized pump and probe light, $\beta_{\parallel}$ refers to the magnetic field component along the laser polarization, while $\beta_{\perp}$ is the modulus of the field perpendicular to the polarization. In analogy with the derivation above, magnetic resonance transitions will then yield a fluorescence signal given by

$$
P_{\text{f}}^{(2)}(\vec{r}) \propto 1 - C^{(2)} \left(\frac{1}{4} + \frac{3}{4} \frac{1 + 8\beta_{\parallel}^2 + 16\beta_{\parallel}^4}{1 + 4\beta_{\parallel}^2 + 4\beta_{\perp}^2} - 3 \frac{\beta_{\parallel}^2 + \beta_{\parallel}^4}{1 + \beta_{\parallel}^2 + \beta_{\perp}^2} \right)
$$
$$
\times \left(1 - \frac{\sqrt{S_{\text{rf}}}}{(\beta_{\text{rf}} - \beta)^2 + S_{\text{rf}} + 1} \right), \tag{13}
$$

with

$$
C^{(2)} = \frac{\alpha^{(2)} \, m_{2,0}^{\text{eq}}}{P_0 \, \kappa_0 L \, \int f^{(2)}(\Omega) \mathrm{d}\Omega}. \tag{14}
$$

4. Experimental apparatus

Figure 1 shows a schematic of the experimental apparatus. In what follows we will refer to a coordinate system, in which the laser beam direction $\vec{k}$ is along $\hat{z}$, the x-axis is along the horizontal direction perpendicular to $\vec{k}$, and $\hat{y}$ is along the vertical direction, the origin of coordinates being chosen in the centre of the spectroscopy cell.

The experiments used 894 nm radiation from a distributed feedback (DFB) laser, whose beam was carried by a single-mode fibre into a optical set-up. The intensity of the collimated beam at the fibre output was ≈ 1 mW. In principle, the frequency stability of the DFB laser was sufficient to carry out the measurements without additional stabilization, but for better performance we actively stabilized the laser frequency to the $F = 4 \rightarrow F' = 3$ hyperfine transition of the caesium D_1 line.

The collimated output beam from the fibre was sent through a combination of $\lambda/2$-plate, polarizer and $\lambda/4$-plate allowing independent control of the laser power and its polarization. For the Bell–Bloom experiment requiring σ_+/σ_--modulation we inserted an electro-optic modulator (Thorlabs, model EO-AM-NR-C1 with model HVA200 driver) before the $\lambda/4$-plate. The EOM was driven by a square wave delivered by a (Keithley, model 3390) waveform generator. The laser beam profile was stretched to an elliptical shape by a cylindrical lens placed after the polarizer, and was then expanded $10\times$ by a spherical lens telescope. Before entering the spectroscopy cell, a narrow vertical strip of the expanded profile was defined by a 1.2 mm wide slit. The beam entering the cell thus had sharply defined boundaries in the direction of observation, while its vertical (y) intensity profile was a Gaussian with a full width at half maximum (FWHM) of 15 mm. The spectroscopy cell was a cubic Pyrex cell (inner volume of $22 \times 22 \times 22$ mm^3) with five optical quality windows containing saturated Cs vapour at ambient temperature together with a mixture of Ar (8 mbar) and Ne (45 mbar) buffer gas, which confined the Cs atoms.

In an auxiliary experiment we have determined the spin coherence relaxation rate in a transmission ground state Hanle experiment (similar to the one described by in [10]), yielding a 2 kHz (HWHM) linewidth. As discussed in section 7, that linewidth becomes significantly narrower when the experiments are performed in a magnetically shielded environment.

Three mutually orthogonal pairs of $(300 \times 300 \text{ mm}^2)$ square Helmholtz coils were used to zero all components of the earth magnetic field. The rf field was produced by two rectangular $(44 \times 100 \text{ mm}^2)$ coils spaced by 22 mm driven by single sine wave or a superposition of sine waves delivered by a programmable (Keithley, model 3390) function generator. When using multi-component rf fields, we accounted for the frequency-dependent impedance of the rf-coil by giving the individual frequency components appropriate voltage amplitudes such as to deliver identical currents to the coils.
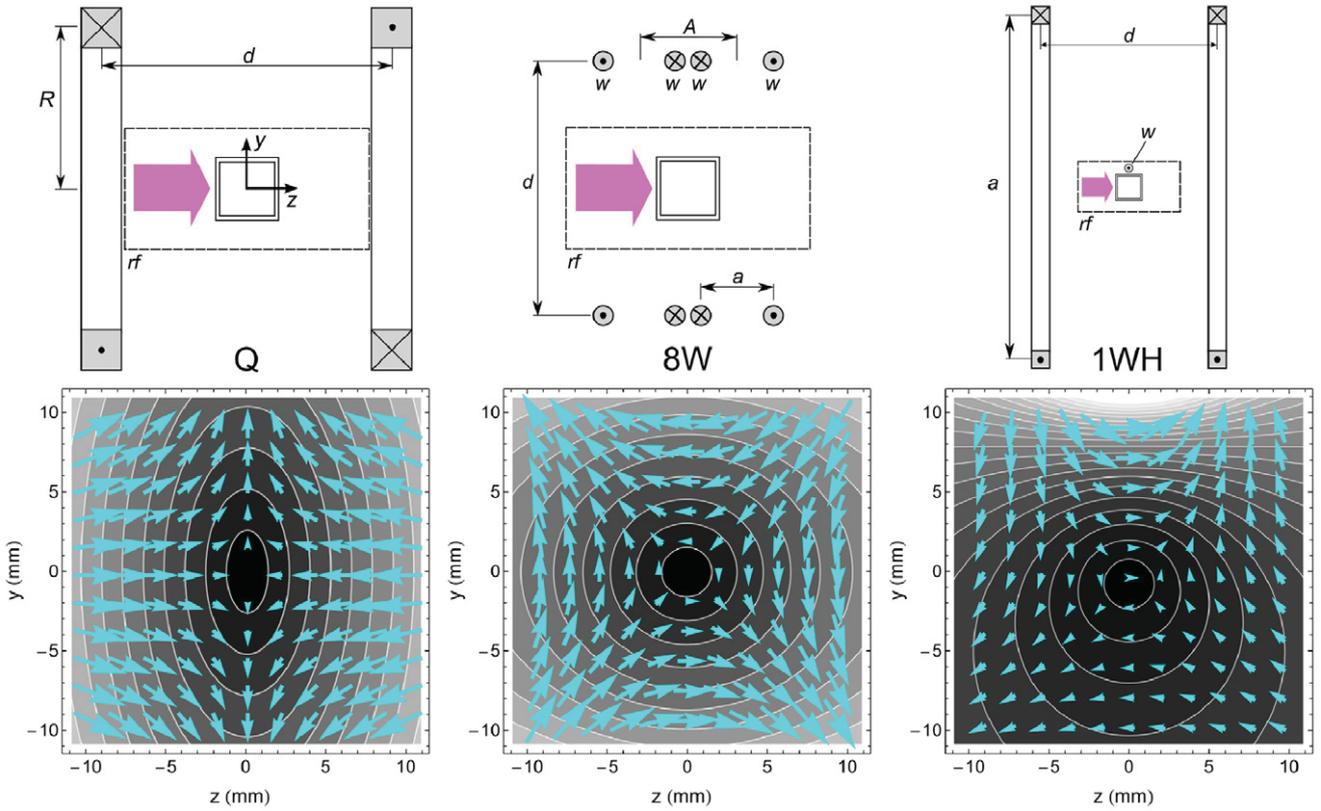
Figure 2. Top row: The three magnetic field configurations studied in this work, shown as cross sections in the $x = 0$ plane. From left to right: Quadrupole (Q), eight wire (8W), and single wire plus Helmholtz (1WH) field configurations. The relative dimensions for each configuration are to scale, except for the wires (w) whose diameters are magnified three times. The cubic spectroscopy cell is located in the centre of each coil arrangement. The dashed rectangles represent the two rf-coils that are offset from the $x = 0$ plane by ± 11 mm. The bottom row shows the calculated contour plots of the magnetic scalar potential in the spatial region covered by the cell, together with superimposed vector plots of the magnetic field lines in the $x = 0$ plane.

For the magnetic field mapping experiments reported below we have produced three types of inhomogeneous fields using three distinct coil and wire configurations as shown in figure 2.

4.1. Quadrupole (Q) field configuration

Two circular coils, are excited by identical currents of opposite sign, thus producing a quadrupole field that is well described by $\vec{B}(\vec{r}) = B_0 (x \, \hat{e}_x + y \, \hat{e}_y - 2z \, \hat{e}_z)$, with $\vec{r} = (x, y, z)$ over the cell dimension. The top graph of the left column in figure 2 shows the Q-configuration, together with the spectroscopy cell. The bottom of the same column shows the magnetic field lines represented by arrows in the $x = 0$ plane (the plane imaged by the CCD camera looking along the x direction), the arrow heads' size representing the magnetic field strength. The field lines are superposed on a contour plot of $|\vec{B}|$; the scalar magnetic equipotential surfaces being ellipsoids with aspect ratios 2 : 1 in the $y-z$ and $x-z$ coordinates; the equipotential lines in the $x = 0$ plane are thus ellipses with the same aspect ratio The characteristic feature of the Q-configuration are constant field gradients dB_z/dz and dB_y/dy with magnitudes in the ratio $-2 : 1$ along the z- and y-axes, respectively.

4.2. Eight-wire (8W) field configuration

Eight long wires arranged as shown in the top of the central column in figure 2 produce homogeneous gradients dB_y/dz and dB_z/dy of equal magnitude, as visualized by the field lines in the lower part of the figure. In the experimental set-up, the wires were 90 mm long copper rods. The iso-potential lines of the 8W-configuration in the $x = 0$ plane in the vicinity of $y = 0$ and $z = 0$ are circles.

4.3. Helmholtz plus single wire (1WH) field configuration

The third field configuration consisted of two square coils in Helmholtz configuration, producing a homogeneous field along $\hat{z}$, onto which the field produced by a single current-carrying wire (w) along $\hat{x}$ is superposed. The sign of the wire current was chosen such as to compensate the homogeneous field at a point near the centre of the cell. Such a field configuration, known as 'z-wire trap' is commonly used for the magnetic trapping of cold atoms on atom chips (see, e.g., [13]) since changing the relative magnitude of the wire and Helmholtz coil currents allows the controlled displacement of the zero-field point along the vertical (y) direction. The coil configuration and a typical field pattern of its non-concentric potential lines are shown in the right column of figure 2.

5

4.4. Data recording and analysis

The laser-induced fluorescence (LIF) from the irradiated Cs vapour layer was imaged by a 16-bit CCD camera (model ST-i monochrome from SBIG Astronomical Instruments, 640×480 pixels), whose line-of-sight was directed along $\hat{x}$ (figure 1). The zoom lens (ARBUS, model TV8553) was adjusted such that an area slightly larger than the (outer) 25×25 mm^2 cross section of the cell was imaged onto the CCD sensor. The LIF intensity variation of interest covered $\approx 10\%$ of the 65'536 grey tones provided by the camera, because of bright regions of scattered light from the lateral windows, as can be seen in the photograph insert of figure 1. We note that with a conventional 8-bit camera that variation would cover only ≈ 25 shades of grey. An 894 nm interference filter mounted on the imaging lens suppressed stray room light.

The typical data recording procedures were as follows: in experiments involving depolarization by rf-irradiation we recorded two images with the same exposure time of typically 20–30 s, namely, one image (main image) with the magnetic field gradient and the rf-field applied to the cell, and one image (reference image) without applied rf-field. For recording the reference image the gradient field was switched off and replaced by a polarization-stabilizing field $\beta_\parallel \gg 1$, oriented along $\hat{k}$ for experiments on oriented atoms, and along the light polarization for experiments on aligned atoms. In an off-line analysis both images were cropped to display only the inner cell cross section of 22×22 mm^2, after which the reference image was subtracted from the main image. The grey tones in the difference image were then rescaled to span the full range from white to black by assigning 0 to the darkest pixel and 1 to the brightest pixel and mapping all intermediate grey tones in a linear manner onto the [0,1] interval.

Based on equation (11a) the differential fluorescence image of *oriented* atoms is thus described by the expression

$$
\delta P_{\mathrm{f}}^{(1)}(\vec{r}) = P_{\mathrm{f}}^{(1)}(\vec{r}, S_{\mathrm{rf}}, \beta_\parallel, \beta_\perp)
$$
$$
- P_{\mathrm{f}}^{(1)}(\vec{r}, S_{\mathrm{rf}} = 0, \beta_\parallel \gg 1, \beta_\perp = 0)
$$
$$
\propto C^{(1)} \Bigg[\frac{1 + \beta_\parallel^2(\vec{r})}{1 + \beta_\parallel^2(\vec{r}) + \beta_\perp^2(\vec{r})}
$$
$$
\times \left(1 - \frac{\sqrt{S_{\mathrm{rf}}}}{[\beta_{\mathrm{rf}} - \beta(\vec{r})]^2 + S_{\mathrm{rf}} + 1} \right) \Bigg], \qquad (15)
$$

where the local magnetic field components $\beta_\parallel$ and $\beta_\perp$, with $\beta = \sqrt{\beta_\parallel^2 + \beta_\perp^2}$ of each voxel at position $\vec{r}$ in the imaged vapour layer determine the fluorescence intensity. Setting $C^{(1)} = 1$ yields images with pixel intensities in the range [0, 1], the same range as covered by the experimental pictures.

In the same way, one derives for the differential fluorescence image of *aligned* atoms

$$
\delta P_{\mathrm{f}}^{(2)}(\vec{r}) = P_{\mathrm{f}}^{(2)}(\vec{r}, S_{\mathrm{rf}}, \beta_\parallel, \beta_\perp)
$$
$$
- P_{\mathrm{f}}^{(2)}(\vec{r}, S_{\mathrm{rf}} = 0, \beta_\parallel \gg 1, \beta_\perp = 0)
$$
$$
\propto C^{(2)} \Bigg[1 - \left(\frac{1}{4} + \frac{3}{4} \frac{1 + 8\beta_\parallel^2 + 16\beta_\parallel^4}{1 + 4\beta_\parallel^2 + 4\beta_\perp^2} - 3 \frac{\beta_\parallel^2 + \beta_\parallel^4}{1 + \beta_\parallel^2 + \beta_\perp^2} \right)
$$
$$
\times \left(1 - \frac{\sqrt{S_{\mathrm{rf}}}}{(\beta_{\mathrm{rf}} - \beta)^2 + S_{\mathrm{rf}} + 1} \right) \Bigg], \qquad (16)
$$

where, as above, $C^{(2)} = 1$ yields images with pixels values spanning the range from 0 (black) to 1 (white).

In the experiment described in section 5.1 that did not use an rf magnetic field, the reference image was recorded by replacing the inhomogeneous magnetic field with a polarization-stabilizing longitudinal field $\beta_\parallel \gg 1 \gg \beta_\perp$. Using equation (6a), one easily sees that the difference image in that case is given by

$$
\delta P_{\mathrm{f}}^{(1)}(\vec{r}) = P_{\mathrm{f}}^{(1)}(\vec{r}, \beta_\parallel, \beta_\perp) - P_{\mathrm{f}}^{(1)}(\vec{r}, \beta_\parallel \gg 1, \beta_\perp = 0)
$$
$$
\propto \frac{\beta_\perp^2(\vec{r})}{1 + \beta_\parallel^2(\vec{r}) + \beta_\perp^2(\vec{r})} . \qquad (17)
$$

The experimental results in the following sections have been modelled by equations (15–17), by adjusting only the rf saturation parameter S_{rf} and the spin relaxation rate γ. In order to account for the inhomogeneous vertical intensity distribution of the laser beam in the cell, the theoretical fluorescence patterns in equations (15–17) were multiplied by a Gaussian $\exp[-y^2/2\sigma_y^2]$ with a FWHM of 15 mm.

5. Experimental results

5.1. Fluorescence of oriented atoms in inhomogeneous magnetic fields

The bottom row of figure 3 shows fluorescence images from the cell excited by circularly polarized light in the three inhomogeneous fields configurations described in section 4. We refer to these fluorescence patterns as 'Hanle background fluorescence' images. The dark horizontal stripes on the fluorescence images are likely due to an interference effect from scattered laser light. Alternatively, the stripes could be shadows or reflections that are produced by small metallic Cs droplets on the windows of the cell.

In the top row we show the corresponding modelled images predicted by equation (17) using the spatial field distributions $\beta_\parallel(\vec{r})$ and $\beta_\perp(\vec{r})$ of the three coil configurations, noting that the subscripts $\parallel$ and $\perp$ refer to the local magnetic field being parallel or perpendicular to the $\hat{k}$-vector of the exciting light beam. The observed and modelled fluorescence patterns show an excellent agreement, except near $\vec{r} = 0$, where the dark spot is slightly less extended in the experimental images, a fact that we assign to laboratory field gradients, noting that, after all, the experiments are carried out in a magnetically unshielded environment. A small contribution from atomic alignment, not taken into account in our model, may also contribute to the slight deviation near $\vec{r} = 0$.

5.2. Fluorescence of rf-depolarized oriented atoms in inhomogeneous magnetic field

Although the results presented in the previous paragraph show a good agreement between observations and the forward model predictions, they are not very useful for addressing the inverse problem that consists in inferring unknown magnetic field distributions from the fluorescence patterns that they produce.

As discussed in section 3.2, the injection of a weak oscillating magnetic field (rf-field) into the cell is a powerful
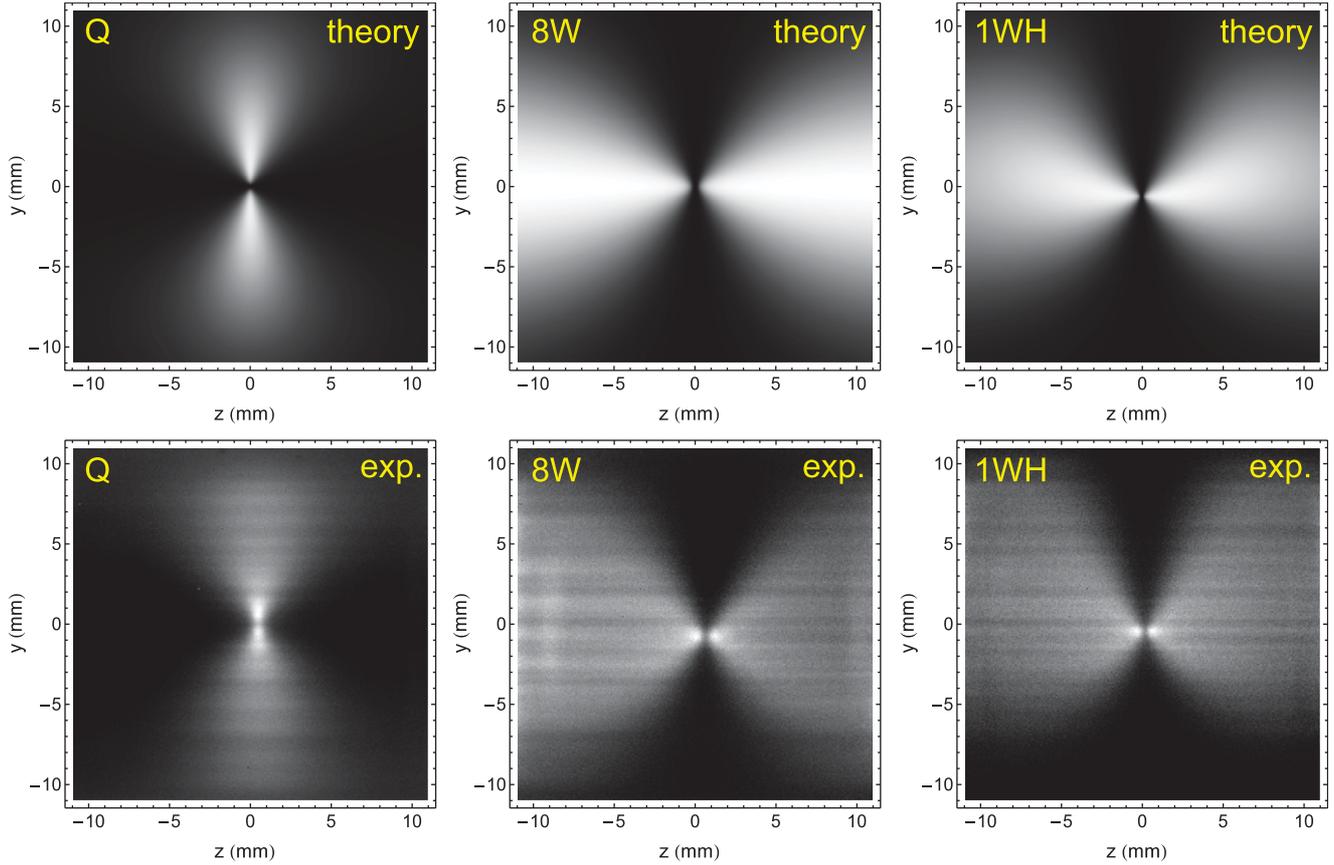
Figure 3. Two-dimensional fluorescence distributions induced by circularly polarized laser light in the three inhomogeneous field configurations shown in figure 2. From left to right: quadrupole field (Q), 8-wire field ($8W$), and Helmholtz plus one-wire field ($1WH$). The top row represents the LIF distribution calculated with equation (6a) and the lower row the experimentally recorded fluorescence patterns.

tool for addressing this inverse problem. Magnetic resonance transitions induced by the rf-field oscillating at ω_{rf} will depolarize atoms at locations where the magnetic resonance condition $\beta = |\vec{\beta}| = \sqrt{\beta_{\parallel}^2 + \beta_{\perp}^2} \equiv \omega_{rf}/\gamma_F$ is fulfilled. This depolarization leads to an enhanced fluorescence intensity, thus highlighting regions of constant magnetic field strength ($\beta = $ const), i.e., yielding bright scalar iso-potential lines. In order to demonstrate this approach we have exposed the cell to an rf-field consisting of a comb of five equidistant harmonic oscillations.

For the Q- and the $1WH$-configurations the rf-field consisted of a fundamental oscillation at $\omega_{rf}/2\pi = 65$ kHz and four harmonics thereof, while the measurements with the $8W$-field involved the fundamental and harmonics of 35 kHz. The graphs in the middle row of figure 4 show the experimental results, in which the bright iso-potential lines clearly stand out against the smooth Hanle background fluorescence pattern. The fluorescence predicted by equation (15) is shown in the top row of figure 4. The results in the top two rows were chosen to illustrate that our model calculations do not only reproduce the bright potential lines, but also the underlying Hanle background fluorescence patterns.

For practical applications one may wish to suppress the Hanle background. This can be achieved by recording the reference image with merely switching off the rf field, and leaving the inhomogeneous field applied. The corresponding results are shown in the bottom row of figure 4.

As an application we show in figure 5 the deformations of the potential lines by a magnetized stainless steel setscrew. The left graph shows a set of iso-field lines in a field produced by the superposition of the (homogeneous) field from a pair of Helmholtz coils and a small linear dB_z/dz-gradient field produced by the quadrupole coil Q. The rf-field for that measurement consisted of a superposition of oscillations at frequencies ranging from 820 to 960 kHz, yielding bright fluorescence lines at fields B_z ranging from 234.3 to 274.3 μT, in steps of 5.7 μT.

When an M4 stainless steel setscrew held by a non-magnetic aluminum rod is approached to the cell from the right side, the iso-potential lines are displaced and deformed as shown on the right graph of figure 5. We show this example merely as a qualitative demonstration of the method. Work on quantitative methods for inferring the field produced by the perturbing object is in progress.

5.3. Fluorescence from rf-depolarized aligned atoms in inhomogeneous magnetic field

We have also recorded fluorescence images induced by *linearly polarized* light that creates an atomic alignment that is then resonantly destroyed by the rf field in a space-selective manner.
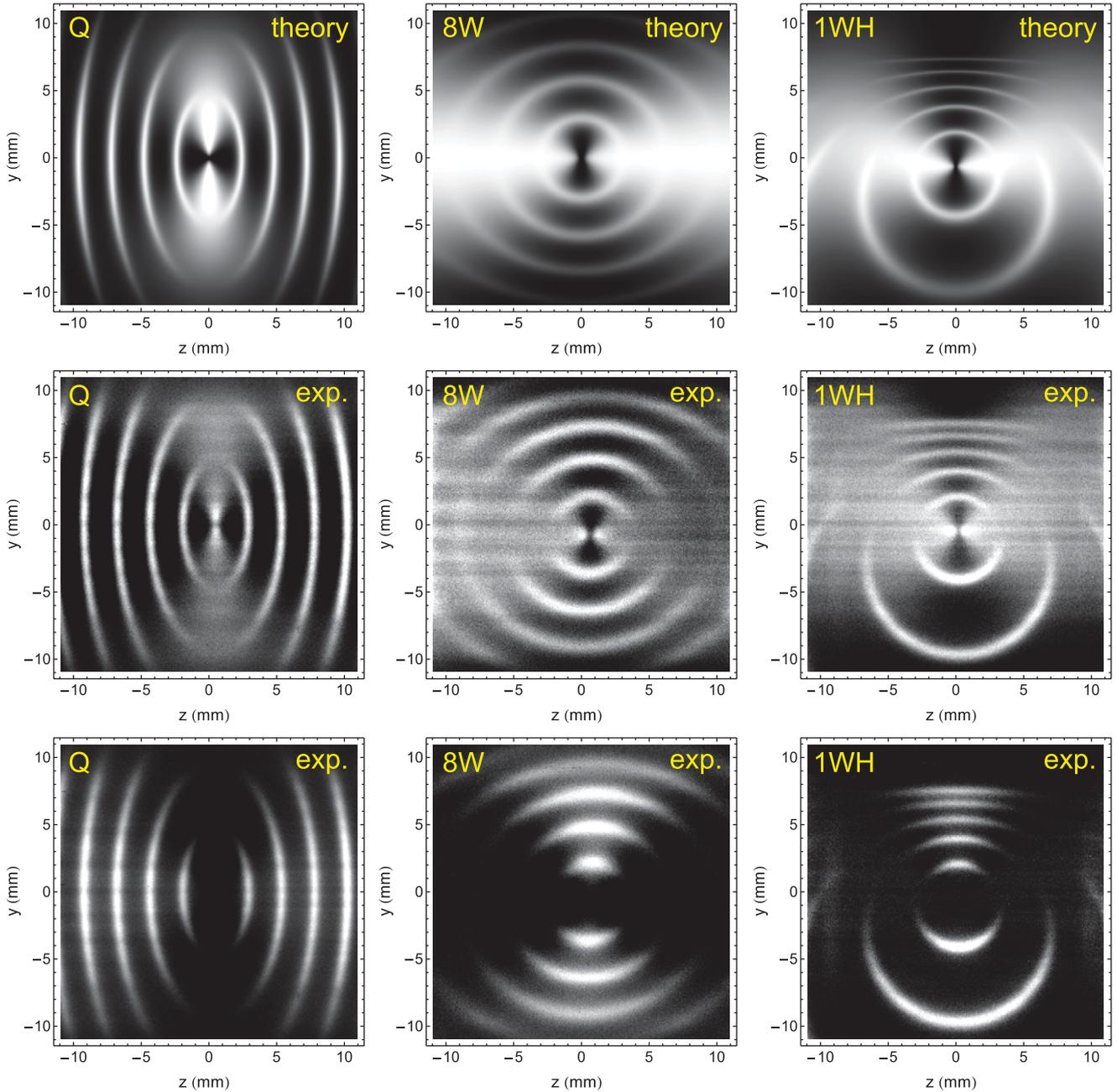
7

Figure 4. Magnetic resonance depolarization of fluorescence induced by *circularly polarized* light in the three inhomogeneous field configurations. A multi-component rf-field used space-selectively depolarizes the atoms, and the bright lines represent scalar magnetic iso-potential lines. For the Q- and the $1WH$-configurations the bright ellipses and circles represent—from inside to outside—lines along which the magnetic field modulus β varies from 19 to 93 μT in steps of 18.5 μT. For the $8W$-configuration the corresponding fields were 10–50 μT (10 μT steps). The top row represents the LIF distributions predicted by equation (15) and the middle row the corresponding measured differential fluorescence patterns. The graphs in the bottom row were produced by subtracting a reference image recorded by switching off the rf field, while leaving the inhomogeneous field applied.

The use of linear polarization introduces an additional degree of freedom, namely, the relative orientation of the direction of polarization and the axis of symmetry (if any) of the gradient producing coils.

Results and their corresponding simulation based on equation (16) are shown in figure 6 for the quadrupole (Q) field and the one-wire plus Helmholtz ($1WH$) field. We find again an excellent agreement between the non-trivial simulated and measured patterns. We note in particular the dark spot in the zero-field point that is particularly well visible in the experiments with x-polarized light. We also note the poorer signal/noise ratio of the experimental data compared to the data obtained with circularly polarized light. This is due to the fact that the buffer gas reduces the optical pumping efficiency with linearly polarized light.

The dependence of the fluorescence maps on the orientation of the light polarization can be understood in a quantitative manner as follows. For the Q-configuration
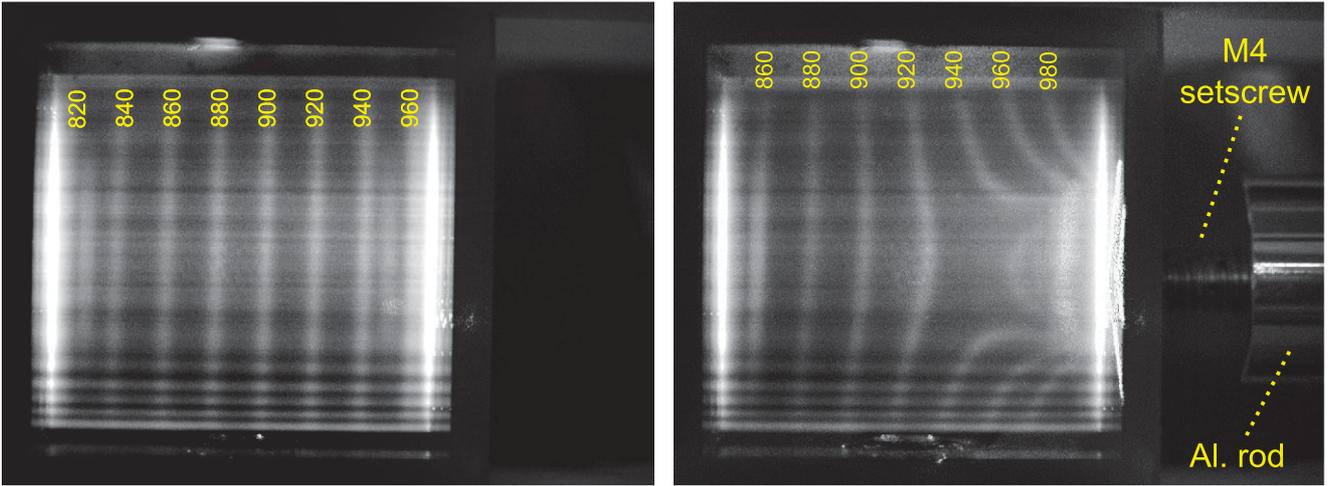
Figure 5. Potential lines in a region with a homogeneous field gradient (left) and deformation of the potential by an M4-setscrew (right).
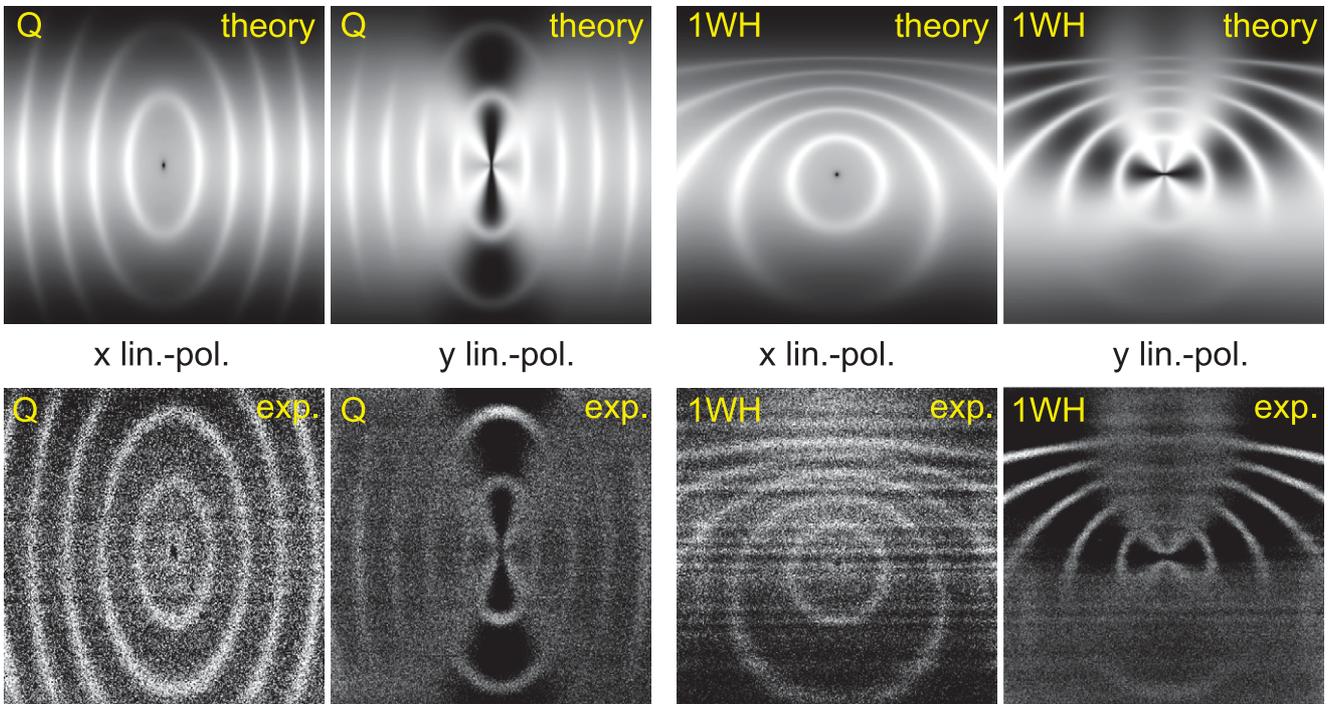

Figure 6. Magnetic resonance depolarization of fluorescence induced by *linearly polarized* light in fields produced by the quadrupole (Q) and one wire plus Helmholtz ($1WH$) coils, respectively. Fluorescence images are shown for laser polarization parallel (x) and perpendicular (y) to the camera's line of sight. A multi-component rf-field consisting of the fundamental and harmonics of 65 kHz is used to space-selectively depolarize atoms. The top row represents the LIF distributions calculated with equation (16) and the lower row recorded the differential fluorescence pattern.

excited, e.g., with y-polarized light figure 2 shows that there is a growing alignment-stabilizing field B_y along the y-direction, hence the dark band of growing width that develops as one moves away (along y) from the centre of the cell. If, on the other hand, the light polarization (in the same Q-configuration) is along x, all field components in the imaged $x = 0$ plane (except for the spot at $y = z = 0$) have a depolarizing effect, hence the overall brighter image. Similar arguments allow one to understand the dark and bright zones in the $8W$ and $1WH$ configurations.

5.4. Dark resonance potential imaging by helicity-modulated light

In 1961 Bell and Bloom have shown [14] that a beam of intensity-modulated light induces magnetic resonance transitions in alkali atoms exposed to a transverse magnetic field when the modulation frequency matches the Larmor precession frequency. Recently we have extended the Bell–Bloom technique to polarization modulation [9, 15] in a transverse magnetic field. When the helicity ξ of a circularly polarized light beam is periodically reversed in synchronicity
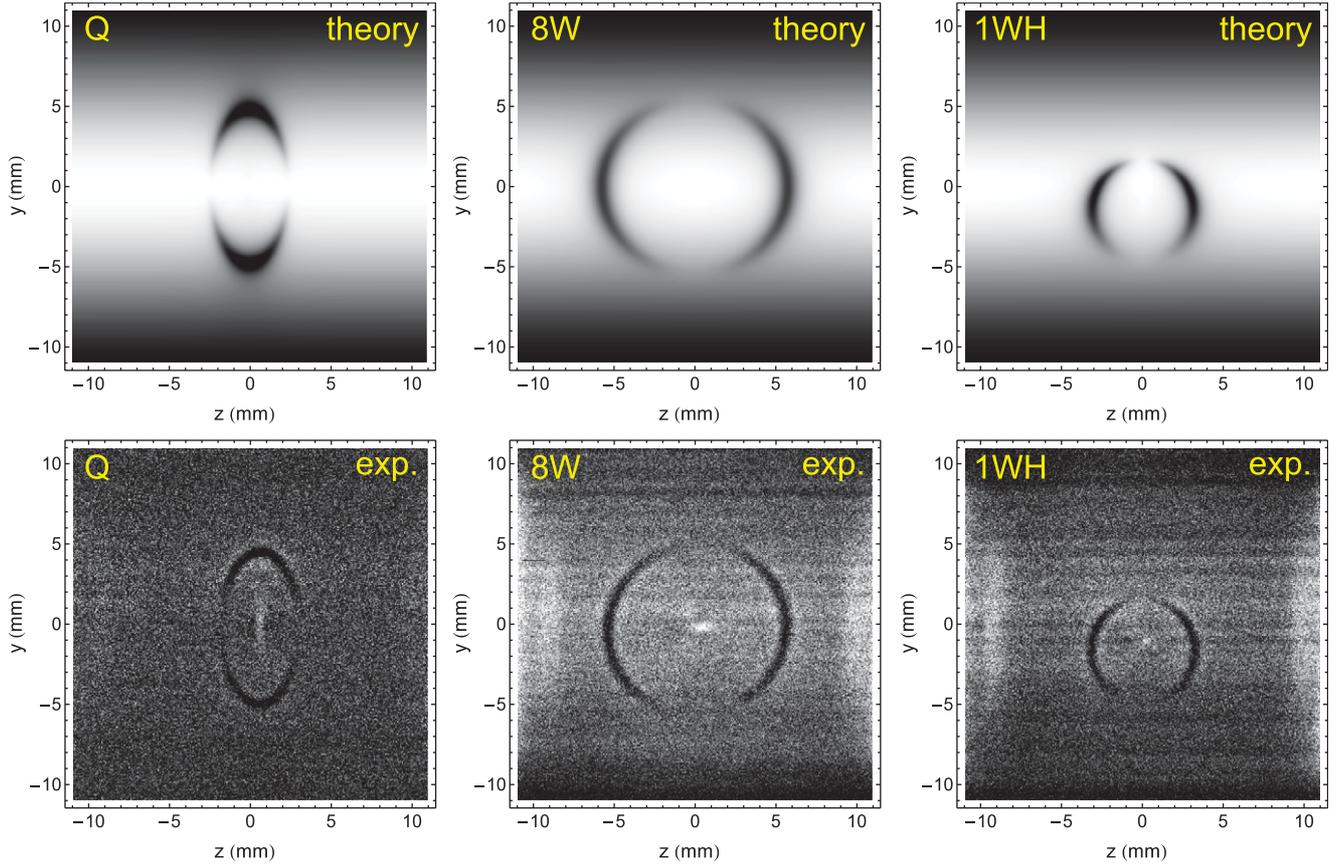
Figure 7. Fluorescence images showing a dark magnetic potential line (superposed on the Hanle background fluorescence) induced by the resonant creation of spin polarization using a light beam with *circular polarization modulation*. Experiments (bottom) were carried out in the three inhomogeneous field configurations $\nu_{mod} = 65\,kHz$ in the Q- and $1WH$-fields, and $35\,kHz$ in the $8W$-field. The top row shows the differential LIF distribution calculated by equation (18).

with the precession of the medium's spin polarization, a resonant build-up of the polarization occurs when the modulation frequency ω_{mod} matches an integer multiple of the Larmor frequency ω_L. This build-up manifest itself as a resonant reduction of the medium's absorption coefficient when $\omega_{mod} = n\omega_L$, and hence a corresponding increase of the transmitted light power [15].

A reduction of the medium's fluorescence is expected to go in pair with this variant of the EIT phenomenon. The graphs in the bottom row of figure 7 show fluorescence images recorded with circular polarization-modulated light in our three standard field configurations. In these recordings the reference image was recorded by switching off the polarization modulator, leaving the light in an unknown (i.e., unmeasured) elliptical polarization state. Since we did not (as for the recordings of figures 4, 6) turn off the gradient field for recording the reference images, the Hanle fluorescence background is suppressed in the differential images.

The experimental images show well the anticipated dark potential line, at positions where the Larmor frequency matches the polarization modulation frequency. With $\omega_{mod}/2\pi = 65\,kHz$ the dark line occurs at a field of $19\,\mu T$ in the Q- and $1WH$-configurations, while it occurs at $10\,\mu T$ in the $8W$-configuration for which $\omega_{mod}/2\pi$ was $35\,kHz$.

On notes the much poorer signal contrast of the (all-optical) modulation experiment compared to the experiments

involving rf-depolarization that is partially due to the square-wave polarization modulation, of which only the fundamental Fourier component contributes. The graphs in the top row of figure 7 show images that were modelled by the function

$$\delta P_{\mathrm{f}}^{(1)}(\vec{r}) \propto 1 - \frac{\beta_{\parallel}^2(\vec{r})}{1 + \beta_{\parallel}^2(\vec{r}) + \beta_{\perp}^2(\vec{r})} \times \frac{1}{[\beta_{mod} - \beta(\vec{r})]^2 + 1}.$$

(18)

applied to all three gradient configurations. In the last expression we have retained only the fundamental Fourier component of the polarization modulation function, since the light intensity was too low to excite the harmonic resonances that are expected to occur at positions $\vec{r}$, where $\omega_{mod} = (n>1)\omega_L(\vec{r})$. These Bell–Bloom dark resonances are complementary to the bright resonances observed with rf-depolarization (figure 4).

6. Spatial resolution and magnetometric sensitivity of field mapping by fluorescence imaging

We estimate the spatial resolution Δz of the iso-potential lines as follows: Suppose that spin-oriented atoms are in a local polarization-stabilizing field, onto which a weak gradient field $G_{zz} = dB_z/dz$ is superposed. The interaction with the rf-field will then depolarize atoms, i.e., make the fluorescence
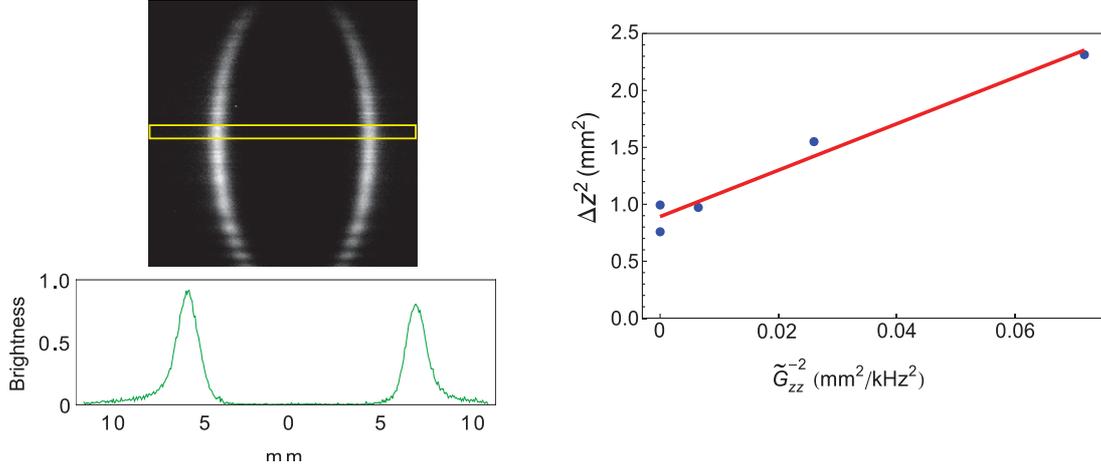
Figure 8. Dependence of the spatial resolution of the fluorescence field imaging method on the applied magnetic field gradient. Left: Typical fluorescence image with single rf-depolarization in Q-gradient field and intensity profile from data in yellow box above. Right: Gradient dependence of the profile widths, together with linear fit.

light up in a region given by $\Delta z = \delta B / G_{zz}$, where δB is the linewidth of the magnetic resonance line. Increasing the gradient G_{zz} will narrow the iso-potential lines, until the region containing depolarized atoms broadens due to the depolarized atoms diffusing out of the depolarization region proper. In very strong gradients the spatial resolution will thus be limited by the distance $\sqrt{2 D \tau}$ over which depolarized atoms diffuse during their spin relaxation time τ, D being the diffusion constant. Since the two effects are statistically independent, we add them quadratically to obtain

$$\Delta z = \sqrt{2 D \tau + (\delta B / G_{zz})^2}. \quad (19)$$

We note that a similar approach was used by Tam [6], who added the two contributions linearly. Inspired by the latter work, we assume the spin relaxation rate to be given by

$$\Gamma = \tau^{-1} = \Gamma_{\text{buffer}} + \Gamma_{\text{pump}} + \gamma_F \, \delta B_{50\,\text{Hz}} \quad (20)$$

where Γ_{buffer} is the depolarization rate due to collisions with buffer gas atoms, and Γ_{pump} the optical pumping, i.e., photon scattering rate. In our unshielded environment laboratory magnetic fields oscillating at the line frequency, artificially broaden the depolarization region, since they jiggle the region in which the rf-depolarization occurs by $\approx 1\,\text{mm}$, as shown below. We parametrize this effect in terms of $\delta B_{50\,\text{Hz}} = \sqrt{\langle B^2(t) \rangle_{\text{rms}}}$ and the corresponding broadening is one to two orders of magnitude larger than Γ_{buffer}. Since the same broadening mechanism determines the width of the magnetic resonance line (an additional contribution from spin-exchange collisions to the latter [6] being completely negligible), we can estimate the field gradient dependence of the spatial resolution to be given by

$$\Delta z \approx \sqrt{\frac{2 D}{\gamma_F \, \delta B_{50\,\text{Hz}} + \Gamma_{\text{pump}}} + \left(\frac{\gamma_F \delta B_{50\,\text{Hz}} + \Gamma_{\text{pump}}}{G_{zz}} \right)^2}, \quad (21)$$

where it is reasonable to assume, although not explicitly proven, that optimal resolution conditions are achieved in the present configuration when Γ_{pump} is on the order of the $50\,\text{Hz}$ broadening term.

Figure 8 represents an experimental recording of the spatial resolution's gradient dependence. For this measurement we varied the value of the gradient in the Q-configuration using a single harmonic oscillation whose frequency was adjusted to produce (for each gradient value) a single equipotential line, such as shown on the top left of figure 8. Cuts through the fluorescence maps (bottom left part of the figure) were then used to infer the FWHM widths Δz of the bright potential lines. The right graph of figure 8 shows the gradient dependence of $(\Delta z)^2$ together with a fit using the model function of equation (21). The intercept at strong gradients yields $\Delta z(G_{zz} \rightarrow \infty) = 0.94(4)\,\text{mm}$. From the slope of the fitted line we infer an effective depolarization rate $\Gamma / 2\pi$ of $4.5(2)\,\text{kHz}$, a value that is compatible with the widths of magnetic resonance lines measured in an auxiliary double resonance transmission experiment.

We estimate the magnetometric resolution of the method in its current implementations as follows: The data in the cuts on the bottom left part of figure 8 represent fluorescence from a voxel of $\approx 1\,\text{mm}^3$, whose signal/noise ratio SNR is ≈ 400. We can thus state that the magnetometric sensitivity is $\delta B_{50\,\text{Hz}} / \gamma_F / SNR \approx 2\,\text{nT}$ with a recording time of $20\,\text{s}$.

7. Summary and outlook

We have presented a tomographic method for mapping two-dimensional distributions of magnetic scalar potentials that is based on the position-selective destruction of spin polarization by magnetic resonance induced by a multi-component oscillating magnetic field. Potential lines are directly visible as CCD camera images, and their contrast can be enhanced by subtraction of suitable reference images. We have also presented algebraic equations that allow the easy forward modelling of the fluorescence pattern for three distinct current geometries used to produce easily calculable inhomogeneous magnetic fields.

The proof-of-principle experiments were carried out in an unshielded environment, where they yield a spatial resolution on the order of 1 mm. The resolution is limited by laboratory

11

magnetic fields oscillating at the line frequency which broaden the magnetic resonance lines to a few kHz. In view of porting the experiments into a magnetically shielded environment we have already determined the magnetic resonance linewidth of the same cell to be on the order of 50 Hz, when recorded in a two-layer magnetic shield. Based on this we expect that a spatial resolution of $\Delta z = \sqrt{D/\Gamma_{\text{pump}}} \approx 100\,\mu\text{m}$ can be achieved when carrying out the experiments (using the same vapour cell) in a shielded environment. Work towards such measurements is in progress. In parallel we work on methods allowing the inverse reconstruction of spatially resolved field patterns from sources with an unknown magnetization.

Acknowledgments

References

[1] Alzetta G, Gozzini A, Moi L and Orriols G 1976 An experimental method for the observation of r.f transitions and laser beat resonances in oriented Na vapour *Nuovo Cimento* B **36** 5–20

[2] Skalla J, Wäckerle G, Mehring M and Pines A 1997 Optical magnetic resonance imaging of Rb vapor in low magnetic fields *Phys. Lett.* A **226** 69–74

[3] Ishikawa K, Anraku Y, Takahashi Y and Yabuzaki T 1999 Optical magnetic-resonance imaging of laser-polarized Cs atoms *J. Opt. Soc. Am.* B **16** 31

[4] Giel D, Hinz G, Nettels D and Weis A 2000 Diffusion of Cs atoms in Ne buffer gas measured by optical magnetic resonance tomography *Opt. Express* **6** 251–6

[5] Tam A C and Happer W 1977 Optically pumped cell for novel visible decay of inhomogeneous magnetic field or of rf frequency spectrum *Appl. Phys. Lett.* **30** 580

[6] Tam A C 1979 Optical pumping of a dense Na+He+N$_2$ system: application as an rf spectrum analyzer *J. Appl. Phys.* **50** 1171–8

[7] Asahi H, Motomura K, Harada K-i and Mitsunaga M 2003 Dark-state imaging for two-dimensional mapping of a magnetic field *Opt. Lett.* **28** 1153–5

[8] Mikhailov E E, Novikova I, Havey M D and Narducci F A 2009 Magnetic field imaging with atomic Rb vapor *Opt. Lett.* **34** 3529–31

[9] Grujić Z D and Weis A 2013 Atomic magnetic resonance induced by amplitude-, frequency-, or polarization-modulated light *Phys. Rev.* A **88** 012508

[10] Castagna N and Weis A 2011 Measurement of longitudinal and transverse spin relaxation rates using the ground-state Hanle effect *Phys. Rev.* A **84** 053421

[11] Breschi E and Weis A 2012 Ground-state Hanle effect based on atomic alignment *Phys. Rev.* A **86** 053427

[12] Bloch F 1946 Nuclear induction *Phys. Rev.* **70** 460–74

[13] Folman R, Krüger P, Schmiedmayer J, Denschlag J and Henkel C 2002 Microscopic atom optics: from wires to an atom chip *Advances In Atomic, Molecular, and Optical Physics* vol 48, ed B Bederson and H Walther (New York: Academic) pp 263–356

[14] Bell W E and Bloom A L 1961 Observation of forbidden resonances in optically driven spin systems *Phys. Rev. Lett.* **6** 623–4

[15] Fescenko I, Knowles P, Weis A and Breschi E 2013 A Bell–Bloom experiment with polarization-modulated light of arbitrary duty cycle *Opt. Express* **21** 15121